

Coarse-Grained Simulation of Bottlebrush: From Single-Chain Properties to Self-Assembly

Juhae Park, Vikram Thapar, Yeojin Choe, Luis Adrian Padilla Salas, Abelardo Ramírez-Hernández,* Juan J. de Pablo,* and Su-Mi Hur*



Cite This: *ACS Macro Lett.* 2022, 11, 1167–1173



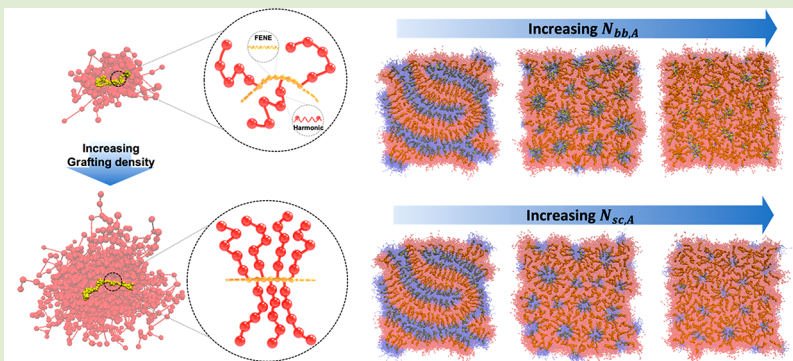
Read Online

ACCESS |

Metrics & More

Article Recommendations

Supporting Information



ABSTRACT: Bottlebrush polymers consist of a linear backbone with densely grafted side chains. They are known to have a range of properties of interest, such as enhanced mechanical strength and rapid self-assembly into large domains, and have attracted attention as promising candidates for applications in photonics, lithography, energy storage, organic optoelectronics, and drug delivery. Here, we present a coarse-grained model of bottlebrush polymers that is able to reproduce their experimentally observed persistence lengths and chain conformations in the melt. The model is then used to investigate the morphologies of this class of materials for various chain architectures and grafting densities.

Bottlebrush polymers exhibit a range of distinctive properties that can be attributed to the underlying chain architecture.¹ The self-assembly of bottlebrush copolymers, in particular, occurs relatively rapidly and is of interest for applications such as photolithography, photonic devices, imaging, and drug delivery.^{2–6} Progress in those applications requires an understanding of the hierarchical organization of these macromolecules, from the chain architecture to the mesoscopic conformation and the supramolecular assembly.^{3,7–12} This multiscale organization represents a challenge for theory and simulations, as it requires to go beyond the chain behavior of individual bottlebrushes. Predictive simulation frameworks must capture molecular-level phenomena, including the emergent stiffness that arises due to side-chain steric repulsion, as well as the microphase separation at much larger scales.

Particle-based models, such as Lennard-Jones (LJ) sites connected by finitely extensible nonlinear elastic (FENE) bonds, have been used before for homopolymer bottlebrush systems in the melt^{10–15} and in solution.^{16–22} Coarse-grained models have also been used to model bottle brush conformation,^{8,10,14,17} but significant challenges remain in the modeling of many-chain collective phenomena occurring over long time and length scales. Pairwise interactions require that

small integration steps be used, leading to a high computational demands. To circumvent this challenge, oversimplified chain architectures have been proposed to adapt particle-based simulations for the study of the self-assembly of bottlebrushes.^{23–25} Such approaches, however, are limited in their ability to describe the wide range of behaviors expected in experiments.

Models with softer interactions such as Self-Consistent Field Theory (SCFT) and field-theoretic simulations, which is highly efficient for large molecules and dense systems, have also been applied to describe bottlebrush systems.^{26–33} Prediction of domain spacing and its scaling on the backbone molecular weight have been some of the major aims for field-theoretic simulations of bottlebrush self-assembly.²⁸ However, predicting backbone stiffness (induced by grafted side chains) and the experimentally observed strong scaling exponents for domain

Received: May 19, 2022

Accepted: August 24, 2022

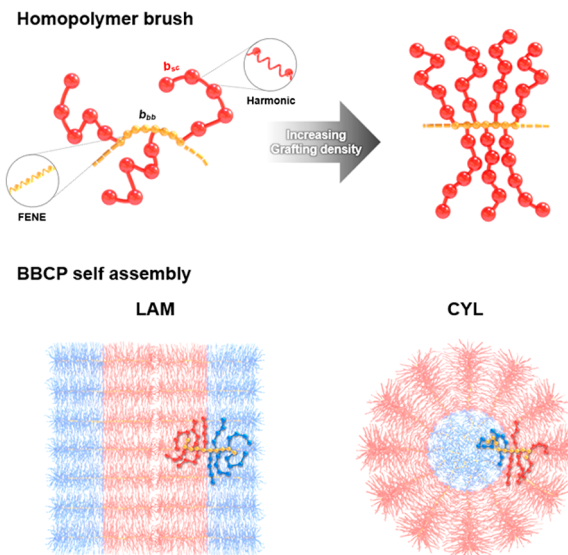
Published: September 9, 2022



spacing in lamellae-forming bottlebrushes is challenging for field-theoretic simulations because they rely on a Gaussian chain model, and densely grafted side chains cause the backbone to stretch, instead of having the side chains stretch radially outward. Dalsin et al. adapted a wormlike chain model for SCFT and predicted a stronger scaling exponent for domain spacing, in agreement with experimental observations.²⁸ The wormlike chain model, however, is unable to describe the nonintrinsic stiffness attributed to the complex chain architecture; instead, the persistence length is predetermined with an adjustable model parameter.

In this work, as illustrated in **Scheme 1**, we propose a coarse-grained simulation model for bottlebrushes, in which the

Scheme 1. (Top) Schematic Illustration of the Coarse-Grained Bottlebrush Polymer Model Consisting of Backbone Beads (Yellow) With FENE Bonds of Averaged Bond Length b_{bb} and Side Chains (Red) Grafted to the Backbone Beads: Each Side Chain Involves N_{sc} Beads with Harmonic Bonds of Average Bond Length b_{sc} ; (Bottom) Cartoon of Self-Assembly (Lamellar LAM and Cylindrical CYL) and Chain Conformation Comparing Bottlebrush Block Copolymers with Different Side-Chain Lengths



emergent chain stiffness caused by the side-chain interactions arises naturally. The usefulness of the approach in predicting bottlebrush copolymers self-assembly is demonstrated by reproducing the scaling behavior of domain spacing in lamellae-forming symmetric bottlebrush block copolymer (BBCP). To complete our study, we also present the predicted phase diagram of BBCPs of varying composition.

The bottlebrush polymers considered here consist of backbones of N_{bb} beads and side chains grafted to selected backbone beads. In our approach, side chains are explicitly modeled with coarse-grained beads connected by a harmonic spring, while the connectivity of the beads in the backbone is described by a FENE potential. The unit length adopted here is the end-to-end distance (R_e) which is commonly used in coarse-grained simulations of block copolymer self-assembly. The average bond length between backbone beads, $b_{bb} = 0.0224R_e$, is chosen to be smaller than that of side chains $b_{sc} = 0.179R_e$. The use of shorter backbone lengths allows us to better capture the stiffness of the bottlebrush. Intra- and

intermolecular nonbonded interactions are expressed as a functional of density fields up to the third order.³⁴ The detailed explanation and model parameters used are provided in the **SI**.

The effects of grafting density (σ , the average number of side chains attached to a backbone bead) and length of side chains (N_{sc}) on backbone stiffness were investigated by performing Monte Carlo (MC) simulations of homopolymer bottlebrushes in the melt state. Simulation details are given in the **SI**. The backbone stiffness is estimated from the decay rate in the bond–bond correlation function of the backbone bonds, $G(l)$, following the procedure outlined by Liang et al.¹⁰ $G(l)$, which quantifies the orientational correlations between unit bond vectors \vec{n}_i and \vec{n}_{i+l} separated by l bonds, is defined as

$$G(l) = \frac{1}{n_{bb} - l} \sum_{i=1}^{n_{bb}-l} \langle (\vec{n}_i \cdot \vec{n}_{i+l}) \rangle \quad (1)$$

where n_{bb} represents the number of bonds in the backbone ($N_{bb} - 1$) and the brackets denote a configuration average. To avoid chain-end effects, the last 10 beads from the ends of the backbone are excluded in the calculation of $G(l)$. **Figure 1a–d** shows calculated $G(l)$ with varying N_{sc} on a semilog scale for $\sigma = 0.25, 0.5, 1.0$, and 2.0 and zoom-in images are also provided in **Figure SI2**. The corresponding curves are fitted with a sum of two exponential functions, which encapsulate both short and long length scaled backbone rigidity induced from local backbone tension and the interaction of side-chains, respectively.¹⁰ From the analytically calculated mean-square end-to-end distance of the backbone, and using the fitted bond–bond correlation function, one can extract an effective Kuhn length (b_k), as shown in **Figure 1e**. At low grafting densities, $\sigma = 0.25$ and 0.5 , $G(l)$ decays rapidly and the effect of N_{sc} on the measured b_k is not significant, since the macromolecules adopt a comb-like architectures with considerable chain flexibility. By increasing σ , b_k sharply increases, and the incremental size becomes pronounced for larger N_{sc} , indicating that the stiffness of the backbone is strongly affected by the steric hindrance induced by the side chains. At $\sigma = 2$, b_k is more than $6\times$ larger than that for $\sigma = 0.25$ for $N_{sc} = 5$. Data presented in **Figure 1e** is collapsed into a universal curve by introducing the crowding parameter (Φ), as shown in **Figure SI3**. The effective Kuhn length follows $b_k \sim b_0$ at low Φ (comb polymer regime) and $b_k \sim \Phi b_0$ at a high Φ (bottlebrush regime).¹⁰

The asymmetry of bottlebrush conformations is presented in **Figure 2a**. The asphericity, a , of the backbone chain, is defined as

$$a = \left\langle \frac{(\lambda_2 - \lambda_1)^2 + (\lambda_3 - \lambda_1)^2 + (\lambda_3 - \lambda_2)^2}{2(\lambda_1 + \lambda_2 + \lambda_3)^2} \right\rangle \quad (2)$$

where the λ s are the eigenvalues of the gyration tensor (where $\lambda_1 < \lambda_2 < \lambda_3$). Ideal spherical conformations have $a = 0$, and $a = 1$ corresponds to rod-like conformations. As inferred from correlation length measurements of bottlebrushes, σ is a significant factor governing backbone conformation. When σ is below 0.25, a weak asphericity is observed, around 0.4; a increases with increasing σ and reaches values above 0.8 at $\sigma = 2.0$. Asphericity increases rapidly at first, and more gradually after $\sigma = 1.0$. Asphericity also increases monotonically as longer side chains are grafted. The dependence on N_{sc} is most prominent at $\sigma = 1.0$. The molecular structure of the side chains can also be investigated by measuring the segmental

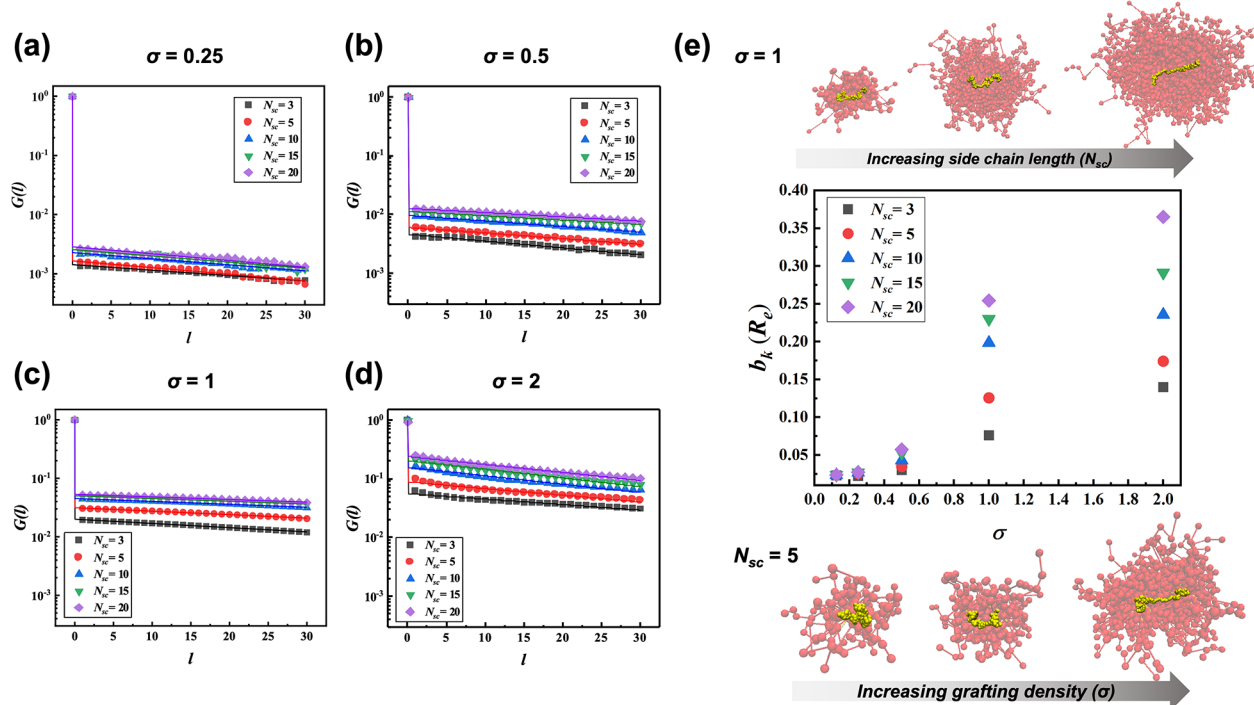


Figure 1. (a–d) Bond–bond correlation function $G(l)$ of bottlebrush homopolymer in the melt with grafting density 0.25, 0.5, 1.0, and 2.0, respectively. An additional $G(l)$ curve at $\sigma = 0.125$ is provided in Figure S11. Bottlebrushes with different side-chain lengths (N_{sc}) of 3, 5, 10, 15, and 20 are compared and denoted on the plot by black squares, red spheres, blue triangles, green inverse triangles, and purple diamonds. The curve of $G(l)$ are fitted with a sum of two exponential functions, shown by solid lines. (e) Estimated effective Kuhn length of the backbone as a function of grafting density. Simulation snapshots of an individual bottlebrush chain with increasing side-chain length and fixed grafting density of 1 are shown on the top, while images of varying grafting density at a fixed $N_{sc} = 5$ are shown in the bottom row.

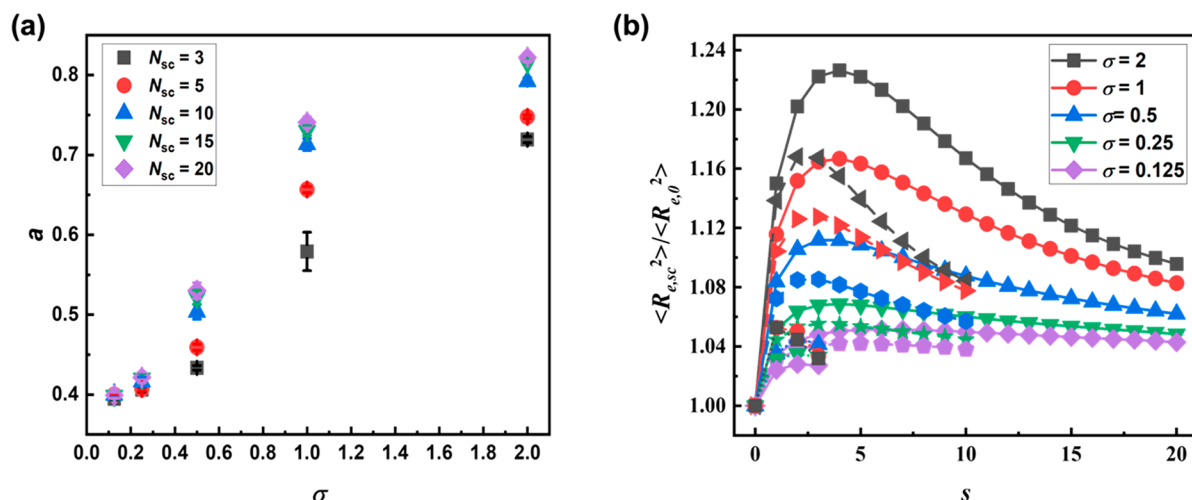


Figure 2. (a) Asphericity of bottlebrush backbone of $N_{bb} = 128$ in the melt for grafting density (σ) and side-chain length (N_{sc}). Black squares, red spheres, blue triangles, green inverse triangles, and purple diamonds represent $N_{sc} = 3, 5, 10, 15$, and 20, respectively. (b) Mean squared section size of bottlebrush side chains from the grafting point to the s^{th} bead relative to the ideal chain of the same length ($\langle R_{e,sc}(s)^2 \rangle / \langle R_{e,0}(s)^2 \rangle$). Black squares, red spheres, blue triangles, green inverse triangles, and purple diamonds represent $\sigma = 2, 1, 0.5, 0.25$, and 0.125. Dotted, dashed, and solid lines correspond to different side-chain lengths, $N_{sc} = 3, 10$, and 20, respectively.

stretching along the contour. Figure 2b shows the mean squared section size of bottlebrush side chains from the grafting point to the s^{th} bead relative to the ideal chain of the same length ($\langle R_{e,sc}(s)^2 \rangle / \langle R_{e,0}(s)^2 \rangle$), where $\langle R_{e,0}(s) \rangle$ is the end-to-end distance of the ideal Gaussian chains with an s degree of polymerization. The extension of the side-chains grows rapidly and peaks below $s = 5$. It then decays smoothly as the block size s increases further. This demonstrates the side-chain

elongation is intensive near the grafting points where the steric hindrance is stronger and released as moving toward the free ends. Our predictions of backbone stiffness and side-chain extension in the proposed model are consistent with previous work with chains of LJ particles connected with FENE bonds.^{10,14} Our results for bottlebrush alignments near the surface (Figure S14) are also consistent with the molecular organization and formation of nematic ordering observed in

experiments and predicted from field-theoretic simulations.^{26,35}

One feature of BBCPs, in which A and B homopolymers are grafted to each block of the backbone, is a stronger scaling exponent γ , around 0.9, for the lamellar period $D^* \sim N_{bb}^\gamma$. This is higher than the $\gamma = 2/3$ value for strongly segregated linear block copolymers.^{7,36,37} In Figure 3a, the measured D^* of symmetric BBCP at $\sigma = 1.0$ and $N_{sc} = 5$ is plotted as a function of N_{bb} in a log–log scale. D^* is calculated when the normal

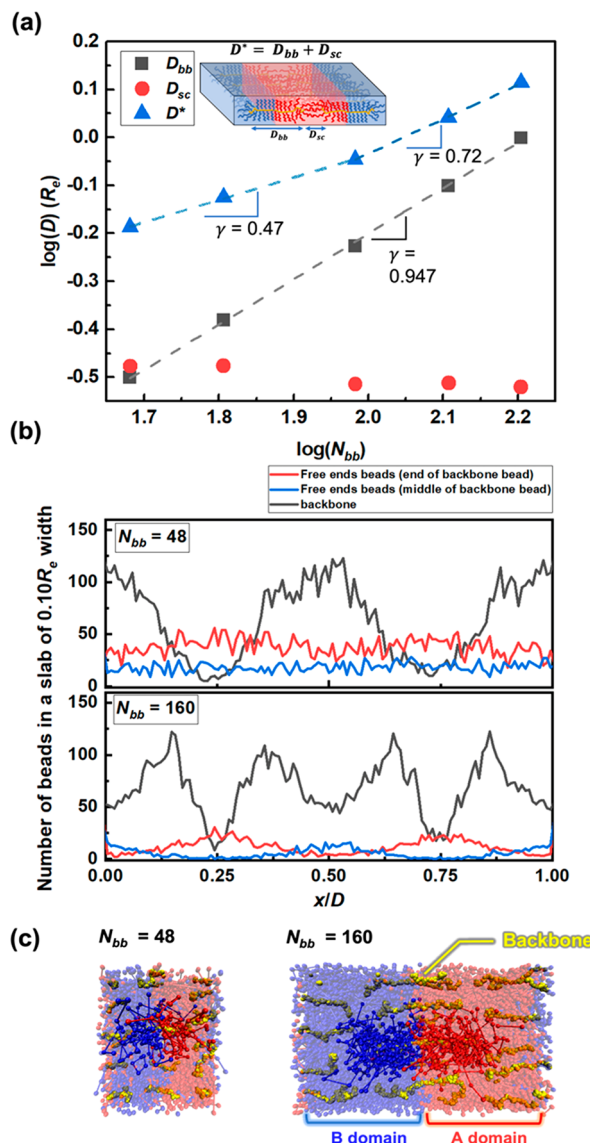


Figure 3. (a) Scaling of lamellae period (D^* in the unit of R_e) of symmetric BBCPs on the backbone length (N_{bb}) in blue triangles. Scaling of the average backbone size perpendicular to the A/B interfaces, D_{bb} , and the size of the side-chain occupied area, D_{sc} , are also included with black squares and red circles. (b) Segmental density distribution of backbones (black) and free ends of side-chains over the lamellar domain (x/D^*) in BBCPs with two values of N_{bb} , namely, 48 and 160. Distribution of free-end beads of side chains grafted to 10 backbone beads located at the ends or middle of the backbone are shown in red and blue, respectively. (c) Simulation snapshots showing chain conformations and the underlying domain size for backbone lengths of $N_{bb} = 48$ and 160. Backbones are highlighted in yellow and side chains from a selected bottlebrush chain are marked with brighter red and blue.

stresses in all direction are equal;³⁸ the measured normal stresses at various L_x and details of the simulation method are provided in Figure S15. In contrast to lamellae of linear block copolymers, BBCP backbones from opposite sides do not interpenetrate strongly in the bilayer arrangement. They are separated by concentrated side chains that are grafted and stretched from the ends of the backbones, as can be appreciated from the nonuniform backbone density distribution (black) over each respective domain, shown in Figure 3b. Figure 3a shows the average backbone size (end-to-end distance) perpendicular to the A/B interfaces D_{bb} , and the size of the side-chain occupied area D_{sc} estimated from $D^* = D_{bb} + D_{sc}$. Regardless of N_{bb} , D_{sc} is almost constant (slightly decaying), while D_{bb} increases as N_{bb} becomes larger, with a scaling exponent of 0.947. However, the formation of side-chain-only domains D_{sc} lowers the scaling exponent for D^* when the molecular weight is relatively low, whereas it approaches one for D_{bb} as N_{bb} becomes large; a star-to-bottlebrush transition is described by the small $\gamma = 0.47$ in the star-like regime and the stronger exponents ($\gamma = 0.72$) in the brush regime of high N_{bb} .

Figure 3b presents the distribution of bottlebrush backbones (black) and free end beads of side chains grafted near the ends (red) or the middle (blue) of the backbone at $N_{bb} = 48$ and 160. For $N_{bb} = 48$, the number density of backbone beads is a smoothly varying function and peaked near the A/B interfaces. However, the free-ends of side chains are uniformly distributed across the domain, regardless to where they are grafted. A BBCP snapshot of $N_{bb} = 48$ in Figure 3c helps illustrate that backbones are not strongly extended outward from the interface, and the chain architectures starts to resemble that of a star-polymer with heteroarms. Consequently, D_{sc} is compatible with D_{bb} , and D^* is governed by the length of the side chains and the backbone; the domain spacing is less dependent on the backbone length. On the other hand, for $N_{bb} = 160$, the backbone density profile shows local minima near the interface and a peak near the edge of the backbone region, indicating the strong extension of the middle blocks perpendicular to the lamellar plane. Thus, the side chains grafted to the middle blocks also take extended conformations parallel to the interface, and their free end distribution shows a peak at the interface. In contrast, the free end density of side-chains grafted to the ends of the backbone peak in the center of side-chain dominant domain, halfway away from the A/B interface. The scaling of D_{bb} is observed to be slightly lower than one because backbone ends have more freedom to fold, as indicated by the higher backbone density at the edges of the backbone-occupied domains. The rich architecture of bottlebrush block copolymer provides additional ways of controlling phase behavior, and their phase diagram has been a topic of considerable interest.^{30,31,39–44} Whereas in linear BCPs the composition is controlled only by the length of each block, bottlebrush block copolymers have additional tunable parameters, including the backbone length of each block, the side-chain lengths, and the grafting densities.³⁹ The overall composition is determined here by either the degree of polymerization of the B block $N_{bb,B}$ or by the length of the grafted B side-chains $N_{sc,B}$, while fixing the total number of backbone beads $N_{bb} = 128$ and the A side-chain length $N_{sc,A} = 5$. Figures 4a and SI6(a) present morphology diagrams for BBCPs with $\sigma = 1.0$ and 2.0, as a function of $N_{bb,B}$ and $N_{sc,B}$. The morphology diagram as a function of f_B and $N_{bb,B}$ is also provided in Figure S17. The f_B value for each condition is

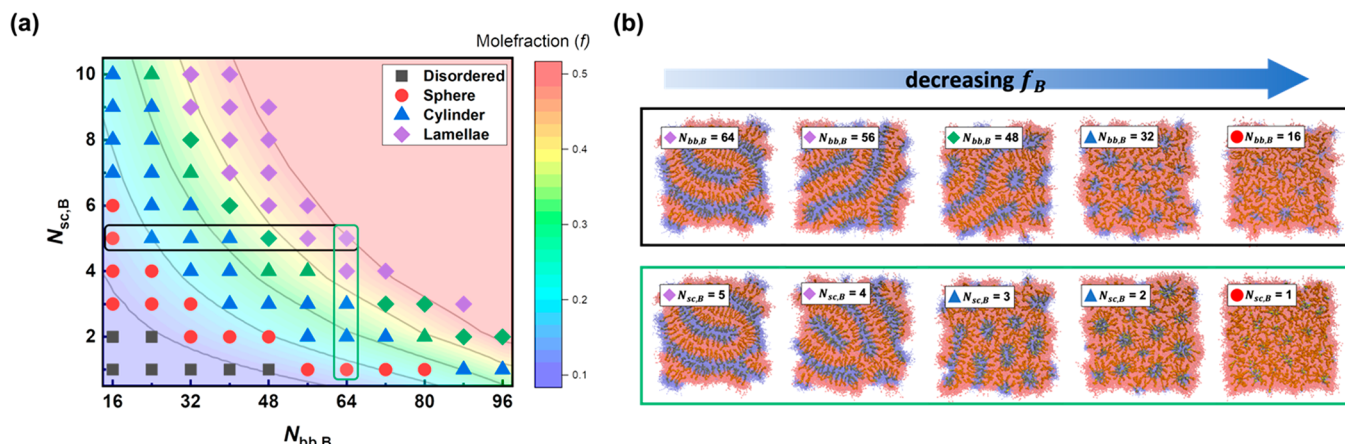


Figure 4. (a) Morphology diagram of bottlebrush block copolymers of varying chain architecture at $\sigma = 1.0$. Black squares, red spheres, blue triangles, and purple diamonds represent disordered, sphere, cylinder, and lamellae phases, respectively. Green-colored symbols indicate the defective structures that form spontaneously in a cubic simulation box; those morphologies are then determined by conducting simulations with a reduced dimension in the z -direction. The color map shows the composition (f_B) with contour curves at $f_B = 0.5, 0.4, 0.3, 0.2$, and 0.1 . (b) Top-views of BBCP morphologies. Red, blue, and yellow beads denote A, B, and C (backbone) beads, respectively. Each row in the black or green boxes corresponds to the horizontal and vertical lines marked in (a).

indicated through the color map and contour curves. Green colors are used where the morphology is identified from additional simulations in a reduced z -dimension of $1R_e$, while the rest of bulk simulations are conducted in a cubic box of $L_x = L_y = L_z = 4R_e$. While detailed studies on the stability of bicontinuous phases are not pursued in this work, a gyroid phase has been demonstrated to occur.^{31,41,45}

A lamellar phase is observed for perfectly symmetric BBCPs of $N_{bb,B} = 64$ and $N_{sc,B} = 5$; cylindrical and spherical morphologies are observed for asymmetric f_B , as expected. The observed morphology evolution of the lamellar phase is provided in Figure S18. The lamellar-to-cylinder transition occurs when f_B is between 0.35–0.4, depending on the chain architecture. The phase window for lamellar morphologies is expanded toward the lower f_B range and lamellae of asymmetric domain sizes can be more easily achieved for $\sigma = 2.0$ (Figure S16(a)). As $N_{bb,B}$ is decreased along the horizontal line in Figure 4a (black box), the lamellae transit into cylinders at low composition, around $f_B = 0.35$, due to the preference for the formation of flat interfaces related to the stiff backbone. On the other hand, when f_B is lowered by decreasing the B side-chain lengths along the vertical direction (green box), cylinders start to appear at a relatively higher value of $f_B \sim 0.40$, as shorter B side chains reduce the steric hindrance and release the backbone stiffness of that block. Further reducing f_B gives rise to phases with more curved interfaces, spheres, and eventually, for extremely small f_B , ordered phases disappear. Figure S17 shows that the order–order transition occurs at different compositions f_B , depending on how to control the composition either by $N_{sc,B}$ or $N_{bb,B}$; for small $N_{bb,B}$ and large $N_{sc,B}$, the transition composition shift to the left. Snapshots of top views from simulations for a reduced film thickness in Figure 4b show the detailed chain conformations and relevant morphologies. When the backbone ratio between blocks is controlled, backbones with a large bending penalty are located perpendicular to the A/B interface, even in cylinders and spheres. Curve interfaces are accommodated by stretching/compression of side chains, and the energy penalty is compensated by reducing A/B contacts. In the center of cylinders and spheres, there exists a

domain occupied mainly by side chains similar to the D_{sc} domains in the lamellar phase. Whereas in the system of symmetric backbone ratio and asymmetric side-chain lengths, shown in the bottom row of Figure 4b, backbones inside the curved domain take a more bent shape reaching the center of cylinders. It is noticeable that the cylinders and spheres of BBCPs have weak packing and nonuniform size distribution. As seen in the snapshots of sphere morphologies at asymmetric backbone ratio and side-chain lengths in Figure S19, only a handful of bottlebrush chains are involved in a cylinder or sphere, and small fluctuation in that numbers causes a pronounced variation of the domain size.

The bottlerush model adopted here consists of explicit polymer chains with beads connected by springs, and with nonbonded interactions described in terms of a functional of the density fields. Side-chain connectivity is modeled with a harmonic potential, and backbone bead connections are represented with the FENE potential. The model is validated by reproducing the persistence length and chain conformations of homopolymer bottlebrush melts of varying grafting densities and side-chain lengths, along with geometric factors for the average size of side-chains, asphericity of bottlebrushes and the nematic order in a film state. The model is able to describe the self-assembly of BBCPs and their sizes for a variety of chain architectures and grafting densities. The model reproduces the strong scaling of the lamellar domain size with molecular weight, and explains the scaling behavior in accordance with the underlying chain conformations and the density distributions. With that model, it was possible to generate phase diagrams of BBCPs that help rationalize the relationship between the underlying BBCP molecular architecture and the resulting self-assembled morphologies. We anticipate that our model will find use in further investigations of BBCPs as a function of chain architecture and composition, including studies of their dynamics, and that it will enable design of engineered structures for advanced applications.

■ ASSOCIATED CONTENT

SI Supporting Information

The Supporting Information is available free of charge at <https://pubs.acs.org/doi/10.1021/acsmacrolett.2c00310>.

Detailed values of model parameters used, bond–bond correlation function with grafting density of 0.125, zoom-plot of bond–bond correlation function, effective Kuhn length as a function of crowding parameter, nematic order of the backbone of homopolymer bottlebrushes near the free surface, morphology map of BBCP at a grafting density of 2.0, morphology diagram as a function of mole fraction and number of segments in the B block at a grafting density of 1.0, evolution of morphologies in BBCPs, and the chain conformations in sphere morphologies of BBCPs ([PDF](#))

■ AUTHOR INFORMATION

Corresponding Authors

Su-Mi Hur — Department of Polymer Engineering, Graduate School, Chonnam National University, Gwangju 61186, Korea; School of Polymer Science and Engineering, Chonnam National University, Gwangju 61186, Korea;  orcid.org/0000-0002-6101-3142; Email: shur@chonnam.ac.kr

Juan J. de Pablo — Pritzker School of Molecular Engineering, The University of Chicago, Chicago, Illinois 60637, United States;  orcid.org/0000-0002-3526-516X; Email: depablo@uchicago.edu

Abelardo Ramírez-Hernández — Department of Biomedical Engineering and Chemical Engineering, The University of Texas at San Antonio, San Antonio, Texas 78249, United States;  orcid.org/0000-0002-3569-5223; Email: abelardo.ramirez-hernandez@utsa.edu

Authors

Juhae Park — Department of Polymer Engineering, Graduate School, Chonnam National University, Gwangju 61186, Korea; Pritzker School of Molecular Engineering, The University of Chicago, Chicago, Illinois 60637, United States

Vikram Thapar — School of Polymer Science and Engineering, Chonnam National University, Gwangju 61186, Korea;  orcid.org/0000-0002-5415-3737

Yeojin Choe — Department of Polymer Engineering, Graduate School, Chonnam National University, Gwangju 61186, Korea; School of Polymer Science and Engineering, Chonnam National University, Gwangju 61186, Korea

Luis Adrian Padilla Salas — School of Polymer Science and Engineering, Chonnam National University, Gwangju 61186, Korea

Complete contact information is available at:
<https://pubs.acs.org/10.1021/acsmacrolett.2c00310>

Notes

The authors declare no competing financial interest.

■ ACKNOWLEDGMENTS

This work is supported by National Research Foundation (NRF) Grant of the Korean Government (Nos. 2021R1A2C1008861 and 2018R1A5A1025224). J. J. de Pablo is grateful for financial support from the Department of Energy, Basic Energy Sciences, Division of Materials Science and Engineering.

■ REFERENCES

- (1) Verduzco, R.; Li, X.; Pesek, S. L.; Stein, G. E. Structure, function, self-assembly, and applications of bottlebrush copolymers. *Chem. Soc. Rev.* **2015**, *44* (8), 2405–2420.
- (2) Sun, G.; Cho, S.; Clark, C.; Verkhoturov, S. V.; Eller, M. J.; Li, A.; Pavia-Jimenez, A.; Schweikert, E. A.; Thackeray, J. W.; Trefonas, P.; Wooley, K. L. Nanoscopic cylindrical dual concentric and lengthwise block brush terpolymers as covalent preassembled high-resolution and high-sensitivity negative-tone photoresist materials. *J. Am. Chem. Soc.* **2013**, *135* (11), 4203–4206.
- (3) Daniel, W. F.; Burdyńska, J.; Vatankhah-Varnoosfaderani, M.; Matyjaszewski, K.; Paturej, J.; Rubinstein, M.; Dobrynin, A. V.; Sheiko, S. S. Solvent-free, supersoft and superelastic bottlebrush melts and networks. *Nature materials* **2016**, *15* (2), 183–189.
- (4) Miyake, G. M.; Piunova, V. A.; Weitekamp, R. A.; Grubbs, R. H. Precisely Tunable Photonic Crystals From Rapidly Self-Assembling Brush Block Copolymer Blends. *Angew. Chem., Int. Ed.* **2012**, *51* (45), 11246–11248.
- (5) Miki, K.; Kimura, A.; Oride, K.; Kuramochi, Y.; Matsuoka, H.; Harada, H.; Hiraoka, M.; Ohe, K. High-Contrast Fluorescence Imaging of Tumors In Vivo Using Nanoparticles of Amphiphilic Brush-Like Copolymers Produced by ROMP. *Angew. Chem., Int. Ed.* **2011**, *50* (29), 6567–6570.
- (6) Kim, N. Y.; Moon, J.; Ryoo, M. H.; Kim, S. H.; Kim, J. H.; Kim, J. M.; Bang, J.; Lee, S. Y. Amphiphilic Bottlebrush Polymeric Binders for High-Mass-Loading Cathodes in Lithium-Ion Batteries. *Adv. Energy Mater.* **2022**, *12* (1), 2102109.
- (7) Lin, T.-P.; Chang, A. B.; Luo, S.-X.; Chen, H.-Y.; Lee, B.; Grubbs, R. H. Effects of grafting density on block polymer self-assembly: From linear to bottlebrush. *ACS Nano* **2017**, *11* (11), 11632–11641.
- (8) Paturej, J.; Sheiko, S. S.; Panyukov, S.; Rubinstein, M. Molecular structure of bottlebrush polymers in melts. *Sci. Adv.* **2016**, *2* (11), No. e1601478.
- (9) Jungmann, P.; Kreer, T.; Sommer, J.-U.; Paturej, J. Conformational properties of end-grafted bottlebrush polymers. *Macromolecules* **2021**, *54* (1), 161–169.
- (10) Liang, H.; Cao, Z.; Wang, Z.; Sheiko, S. S.; Dobrynin, A. V. Combs and Bottlebrushes in a Melt. *Macromolecules* **2017**, *50* (8), 3430–3437.
- (11) Liang, H.; Wang, Z.; Sheiko, S. S.; Dobrynin, A. V. Comb and bottlebrush graft copolymers in a melt. *Macromolecules* **2019**, *52* (10), 3942–3950.
- (12) Liang, H.; Wang, Z.; Dobrynin, A. V. Scattering from melts of combs and bottlebrushes: Molecular dynamics simulations and theoretical study. *Macromolecules* **2019**, *52* (15), 5555–5562.
- (13) Borodinov, N.; Belianinov, A.; Chang, D.; Carrillo, J.-M.; Burch, M. J.; Xu, Y.; Hong, K.; Ievlev, A. V.; Sumpter, B. G.; Ovchinnikova, O. S. Molecular reorganization in bulk bottlebrush polymers: direct observation via nanoscale imaging. *Nanoscale* **2018**, *10* (37), 18001–18009.
- (14) Cao, Z.; Carrillo, J.-M. Y.; Sheiko, S. S.; Dobrynin, A. V. Computer simulations of bottle brushes: From melts to soft networks. *Macromolecules* **2015**, *48* (14), 5006–5015.
- (15) Chremos, A.; Douglas, J. F. A comparative study of thermodynamic, conformational, and structural properties of bottlebrush with star and ring polymer melts. *J. Chem. Phys.* **2018**, *149* (4), 044904.
- (16) Chatterjee, D.; Vilgis, T. A. Scaling Laws of Bottle-Brush Polymers in Dilute Solutions. *Macromol. Theory Simul.* **2016**, *25* (6), 518–523.
- (17) Dutta, S.; Wade, M. A.; Walsh, D. J.; Guironnet, D.; Rogers, S. A.; Sing, C. E. Dilute solution structure of bottlebrush polymers. *Soft Matter* **2019**, *15* (14), 2928–2941.
- (18) Theodorakis, P. E.; Hsu, H.-P.; Paul, W.; Binder, K. Computer simulation of bottle-brush polymers with flexible backbone: Good solvent versus theta solvent conditions. *J. Chem. Phys.* **2011**, *135* (16), 164903.

- (19) Lyubimov, I.; Wessels, M. G.; Jayaraman, A. Molecular dynamics simulation and PRISM theory study of assembly in solutions of amphiphilic bottlebrush block copolymers. *Macromolecules* **2018**, *51* (19), 7586–7599.
- (20) Wessels, M. G.; Jayaraman, A. Molecular dynamics simulation study of linear, bottlebrush, and star-like amphiphilic block polymer assembly in solution. *Soft Matter* **2019**, *15* (19), 3987–3998.
- (21) Hsu, H. P.; Paul, W.; Binder, K. Understanding the Multiple Length Scales Describing the Structure of Bottle-brush Polymers by Monte Carlo Simulation Methods. *Macromol. Theory Simul.* **2011**, *20* (7), 510–525.
- (22) Hsu, H.-P.; Paul, W.; Rathgeber, S.; Binder, K. Characteristic length scales and radial monomer density profiles of molecular bottlebrushes: Simulation and experiment. *Macromolecules* **2010**, *43* (3), 1592–1601.
- (23) Pan, T.; Patel, B. B.; Walsh, D. J.; Dutta, S.; Guironnet, D.; Diau, Y.; Sing, C. E. Implicit Side-Chain Model and Experimental Characterization of Bottlebrush Block Copolymer Solution Assembly. *Macromolecules* **2021**, *54* (8), 3620–3633.
- (24) Chremos, A.; Theodorakis, P. E. Morphologies of bottle-brush block copolymers. *ACS Macro Lett.* **2014**, *3* (10), 1096–1100.
- (25) Sunday, D. F.; Chang, A. B.; Liman, C. D.; Gann, E.; Delongchamp, D. M.; Thomsen, L.; Matsen, M. W.; Grubbs, R. H.; Soles, C. L. Self-Assembly of ABC bottlebrush Triblock Terpolymers with evidence for Looped backbone conformations. *Macromolecules* **2018**, *51* (18), 7178–7185.
- (26) Panagiotou, E.; Delaney, K. T.; Fredrickson, G. H. Theoretical prediction of an isotropic to nematic phase transition in bottlebrush homopolymer melts. *J. Chem. Phys.* **2019**, *151* (9), 094901.
- (27) Levi, A. E.; Lequeieu, J.; Horne, J. D.; Bates, M. W.; Ren, J. M.; Delaney, K. T.; Fredrickson, G. H.; Bates, C. M. Miktoarm Stars via Grafting-Through Copolymerization: Self-Assembly and the Star-to-Bottlebrush Transition. *Macromolecules* **2019**, *52* (4), 1794–1802.
- (28) Dalsin, S. J.; Rions-Maehren, T. G.; Beam, M. D.; Bates, F. S.; Hillmyer, M. A.; Matsen, M. W. Bottlebrush block polymers: Quantitative theory and experiments. *ACS Nano* **2015**, *9* (12), 12233–12245.
- (29) Spencer, R. K.; Matsen, M. W. Field-theoretic simulations of bottlebrush copolymers. *J. Chem. Phys.* **2018**, *149* (18), 184901.
- (30) Gadelrab, K. R.; Alexander-Katz, A. Effect of molecular architecture on the self-assembly of bottlebrush copolymers. *J. Phys. Chem. B* **2020**, *124* (50), 11519–11529.
- (31) Park, S. J.; Cheong, G. K.; Bates, F. S.; Dorfman, K. D. Stability of the Double Gyroid Phase in Bottlebrush Diblock Copolymer Melts. *Macromolecules* **2021**, *54* (19), 9063–9070.
- (32) Cheng, L.-C.; Gadelrab, K. R.; Kawamoto, K.; Yager, K. G.; Johnson, J. A.; Alexander-Katz, A.; Ross, C. A. Templated self-assembly of a PS-branch-PDMS bottlebrush copolymer. *Nano Lett.* **2018**, *18* (7), 4360–4369.
- (33) Chen, Y.; Zhang, X.; Jiang, Y. The influence of side-chain conformations on the phase behavior of bottlebrush block polymers. *Soft Matter* **2020**, *16* (34), 8047–8056.
- (34) Hömberg, M.; Müller, M. Main phase transition in lipid bilayers: phase coexistence and line tension in a soft, solvent-free, coarse-grained model. *J. Chem. Phys.* **2010**, *132* (15), 155104.
- (35) Mah, A. H.; Laws, T.; Li, W.; Mei, H.; Brown, C. C.; Ievlev, A.; Kumar, R.; Verduzco, R.; Stein, G. E. Entropic and enthalpic effects in thin film blends of homopolymers and bottlebrush polymers. *Macromolecules* **2019**, *52* (4), 1526–1535.
- (36) Rzayev, J. Synthesis of polystyrene- polylactide bottlebrush block copolymers and their melt self-assembly into large domain nanostructures. *Macromolecules* **2009**, *42* (6), 2135–2141.
- (37) Gu, W.; Huh, J.; Hong, S. W.; Sveinbjörnsson, B. R.; Park, C.; Grubbs, R. H.; Russell, T. P. Self-assembly of symmetric brush diblock copolymers. *ACS Nano* **2013**, *7* (3), 2551–2558.
- (38) Detcheverry, F. A.; Kang, H.; Daoulas, K. C.; Müller, M.; Nealey, P. F.; de Pablo, J. J. Monte Carlo simulations of a coarse grain model for block copolymers and nanocomposites. *Macromolecules* **2008**, *41* (13), 4989–5001.
- (39) Gai, Y.; Song, D.-P.; Yavitt, B. M.; Watkins, J. J. Polystyrene-block-poly(ethylene oxide) Bottlebrush Block Copolymer Morphology Transitions: Influence of Side Chain Length and Volume Fraction. *Macromolecules* **2017**, *50* (4), 1503–1511.
- (40) Zhulina, E. B.; Sheiko, S. S.; Dobrynin, A. V.; Borisov, O. V. Microphase segregation in the melts of bottlebrush block copolymers. *Macromolecules* **2020**, *53* (7), 2582–2593.
- (41) Jiang, L.; Nykypanchuk, D.; Pastore, V. J.; Rzayev, J. Morphological Behavior of Compositionally Gradient Polystyrene-Polylactide Bottlebrush Copolymers. *Macromolecules* **2019**, *52* (21), 8217–8226.
- (42) Song, D.-P.; Gai, Y.; Yavitt, B. M.; Ribbe, A.; Gido, S.; Watkins, J. J. Structural Diversity and Phase Behavior of Brush Block Copolymer Nanocomposites. *Macromolecules* **2016**, *49* (17), 6480–6488.
- (43) Gai, Y.; Song, D.-P.; Yavitt, B. M.; Watkins, J. J. Polystyrene-block-poly (ethylene oxide) bottlebrush block copolymer morphology transitions: Influence of side chain length and volume fraction. *Macromolecules* **2017**, *50* (4), 1503–1511.
- (44) Chang, A. B.; Bates, F. S. Impact of Architectural Asymmetry on Frank-Kasper Phase Formation in Block Polymer Melts. *ACS Nano* **2020**, *14* (9), 11463–11472.
- (45) Lequeieu, J.; Quah, T.; Delaney, K. T.; Fredrickson, G. H. Complete photonic band gaps with nonfrustrated ABC bottlebrush block polymers. *ACS Macro Lett.* **2020**, *9* (7), 1074–1080.

□ Recommended by ACS

Topologically Precise and Discrete Bottlebrush Polymers: Synthesis, Characterization, and Structure–Property Relationships

Nduka D. Ogbonna, Jimmy Lawrence, et al.

MARCH 18, 2022

JACS AU

READ ▶

Identifying and Tracking Defects in Dynamic Supramolecular Polymers

Piero Gasparotto, Giovanni M. Pavan, et al.

DECEMBER 30, 2019

THE JOURNAL OF PHYSICAL CHEMISTRY B

READ ▶

Materials Design of Highly Branched Bottlebrush Polymers at the Intersection of Modeling, Synthesis, Processing, and Characterization

Tianyuan Pan, Charles E. Sing, et al.

FEBRUARY 23, 2022

CHEMISTRY OF MATERIALS

READ ▶

Impact of Architectural Asymmetry on Frank–Kasper Phase Formation in Block Polymer Melts

Alice B. Chang and Frank S. Bates

AUGUST 21, 2020

ACS NANO

READ ▶

Get More Suggestions >